Ground State and Hidden Symmetry of Magic-Angle Graphene at Even Integer Filling

Nick Bultinck[1,†], Eslam Khalaf[2,†], Shang Liu[2], Shubhayu Chatterjee[1], Ashvin Vishwanath[2], and Michael P. Zaletel[1,*]

[1]*Department of Physics, University of California, Berkeley, California 94720, USA*
[2]*Department of Physics, Harvard University, Cambridge, Massachusetts 02138, USA*

In magic angle twisted bilayer graphene (TBG), electron-electron interactions play a central role, resulting in correlated insulating states at certain integer fillings. Identifying the nature of these insulators is a central question, and it is potentially linked to the relatively high-temperature superconductivity observed in the same devices. Here, we address this question using a combination of analytical strong-coupling arguments and a comprehensive Hartree-Fock numerical calculation, which includes the effect of remote bands. The ground state we obtain at charge neutrality is an unusual ordered state, which we call the Kramers intervalley-coherent (K-IVC) insulator. In its simplest form, the K-IVC order exhibits a pattern of alternating circulating currents that triples the graphene unit cell, leading to an "orbital magnetization density wave." Although translation and time-reversal symmetry are broken, a combined "Kramers" time-reversal symmetry is preserved. Our analytic arguments are built on first identifying an approximate $U(4) \times U(4)$ symmetry, resulting from the remarkable properties of the TBG band structure, which helps select a low-energy manifold of states that are further split to favor the K-IVC state. This low-energy manifold is also found in the Hartree-Fock numerical calculation. We show that symmetry-lowering perturbations can stabilize other insulators and the semimetallic state, and we discuss the ground state at half-filling and give a comparison with experiments.

I. INTRODUCTION

In twisted bilayer graphene (TBG), two sheets of graphene twisted by a small angle θ create a moiré lattice, resulting in electronic minibands. For a particular "magic" twist angle $\theta \sim 1.05°$, theory predicts that the minibands near charge neutrality (CN) will have minimal dispersion [1,2], and electron-electron interactions play a dominant role. Indeed, when the electron filling ν of these nearly flat bands is varied (completely full or empty bands corresponding to $\nu = \pm 4$ electrons per moiré unit cell relative to charge neutrality), insulating states appear at various integer fillings [3–5]. The nature of these insulators continue to be debated [6–13]. Furthermore, superconductivity is observed on introducing charge carries into the insulating state [4,5,14].

Several aspects of the physics of TBG are reminiscent of multicomponent quantum Hall (QH) systems (e.g., with spin, valley, or layer), where correlated insulators also arise at integer fillings. The driving force in this case is the exchange interaction that spontaneously polarizes the electrons into a subset of the components. The Landau-level form of the single-particle wave functions, which quenches the kinetic energy while preserving their spatial overlap, plays a key role in stabilizing these ferromagnets. However, the addition of the time-reversal symmetry present in TBG, particularly when combined with 180-degree in-plane rotation symmetry (C_2) that effectively enforces time reversal in each valley, opens the door to different orders (including superconductivity) that are absent in the quantum Hall setting. Indeed, TBG is one of the few moiré materials that retains C_2 symmetry, which leads to special properties such as unremovable band touchings that double the number of low-energy modes. Symmetry-lowering perturbations such as an aligned h-BN substrate or weak magnetic fields are known to induce an integer quantum Hall (IQH) insulator in certain cases [15,16].

In the other canonical model of strong-coupling physics, the Mott-Hubbard model, symmetry breaking in the correlated (Mott) insulator is governed by antiferromagnetic superexchange. A pivotal question is whether the single-particle subspace defined by TBG leads to insulators that parallel the quantum Hall case, with a cascade of polarized states, or more closely resembles that in the Hubbard model. We answer this question by considering the structure of Coulomb interactions projected directly into the

k-space continuum model of TBG, including several of the remote bands [10,12,13]. While Mott-Hubbard representations [7,8,17,18] are complicated by the topology of the nearly flat bands [6,11,19–22], one can work directly in the space of the continuum wave functions. Here, careful analysis reveals some generic features of the Coulomb matrix elements that arise from the symmetry and topology of the flat bands. This analysis allows us to identify both an enlarged U(4) × U(4) approximate symmetry group and an intervalley-coherent (IVC) order at neutrality, which were missed in previous approaches.

This "hidden" symmetry of the model has important phenomenological consequences. Experimentally, many of the basic phenomena—such as the existence of correlated insulators at integer fillings, the location of superconducting domes, and the presence of anomalous Hall effects—differ from sample to sample. Since the energetics may depend on parameters like the precise twist angle, alignment with the h-BN substrate, and strain, the search for a "unified" theory of TBG may become mired in a swamp of microscopic details. However, in this work, we identify a hierarchy of energy scales in TBG that can naturally unify many of these findings. Because of the remarkable properties of the TBG band structure, we show that the largest energy scales (15–30 meV) preserve the approximate U(4) × U(4) symmetry, which relates a small number of competing symmetry-breaking orders. Smaller effects (0.2–5 meV) then choose between these orders, and we identify several concrete mechanisms, such as strain or substrate alignment, which can tilt the balance between them.

The primary focus of this work is to understand the implications of this hierarchy at charge neutrality ($\nu = 0$). In certain samples with low twist-angle disorder, an insulating state is observed in transport at $\nu = 0$, even in the absence of apparent hBN alignment [5]. Scanning tunneling microscopy also finds that the density of states (DOS) is reconstructed at $\nu = 0$, where a gap of about 15–30 meV opens up [11,23–25]. We identify this phase as a new Kramers intervalley-coherent (K-IVC) state. In the K-IVC phase (Fig. 1), time reversal is spontaneously broken in each spin component, and a pattern of alternating circulating currents develop which triple the graphene unit cell (the moiré unit cell is unchanged). See Fig. 1 for a graphical illustration of this alternating current order. The K-IVC order does not have a net magnetization; rather, it is a "magnetization density wave" at the wave vector K of graphene's Dirac point. Like an antiferromagnet, the K-IVC preserves a modified time-reversal symmetry $\mathcal{T}'$ combining the regular (spinless) time reversal $\mathcal{T}$ with a π shift in the IVC phase. The new time reversal has the remarkable property that $(\mathcal{T}')^2 = -1$; i.e., it is a Kramers time-reversal symmetry arising from the valley rather than spin. The presence of $\mathcal{T}'$ leads to Kramers pairing in the spectrum, independent of spin, and may have important implications for the nature of superconductivity when the
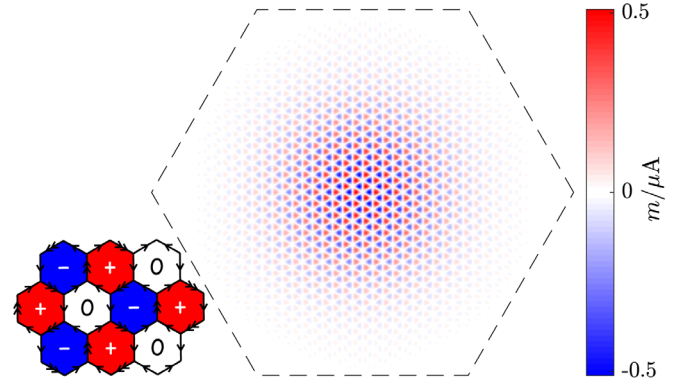

FIG. 1. Circulating currents and magnetization of the K-IVC state. Similar to a Kekule distortion, spontaneous intervalley coherence between the $K - K'$ points of the graphene triples the graphene unit cell. The amplitude of the circulating current slowly modulates over the moiré unit cell, shown here as the magnetization density $m(\mathbf{r})$, while preserving the moiré superlattice translations. We show the contribution from a single spin species summed over the two layers; the other spin carries either identical or reversed currents if the K-IVC state is a spin singlet or spin "triplet," respectively. The lower-left inset shows an example of the circulating current pattern that retains $C_2\mathcal{T}$ symmetry, at the scale of the *graphene* lattice, in the AA region of the moiré unit cell.

K-IVC insulator at $\nu = 0$ is doped. Furthermore, restricting to each spin, the K-IVC state is a topological insulator, though the protecting $\mathcal{T}'$ symmetry may be strongly broken by the edge (due to broken translation symmetry).

Before detailing the Hamiltonian, let us briefly summarize the origin of the approximate U(4) × U(4) symmetry. The eight flat bands are labeled by spin s, valley τ, and a twofold "band" index σ. Since the bands are quite flat, there is no particular reason that σ should label the single-particle eigenbasis. Instead, it turns out that the two bands can be decomposed into a Chern $C = 1$ band and a $C = -1$ band related by $C_2\mathcal{T}$ symmetry, leading to a total of four $C = 1$ and four $C = -1$ bands. Remarkably, the wave functions in the Chern basis have a substantial sublattice polarization; i.e., they have a larger projection on one sublattice compared to the other. Thus, we can label them by $\sigma_z = A/B = \pm 1$ with the Chern number $C = \sigma_z\tau_z$. Because of this sublattice polarization, the slowly varying part of the charge density decouples, to a good approximation, into the two Chern components: $n(r) = n_{C=1}(r) + n_{C=-1}(r)$ (otherwise, there would be large cross terms). The four $C = 1$ ($C = -1$) wave functions are almost identical up to a permutation of the spin and sublattice, so $n(r)$, and hence the interaction, is invariant under separate U(4) rotations acting on the $C = 1/-1$ components. The single-particle dispersion and other perturbations then weakly break this symmetry down to the physical one.

This case is, in fact, highly reminiscent of the QH effect in the zeroth Landau level (ZLL) of monolayer graphene, which also has a sublattice-valley locking $\sigma_z\tau_z = \text{sgn}(B)$,

which leads to an approximate U(4) symmetry. Indeed, TBG is, in essence, two time-reversed copies of the ZLL of MLG: $\sigma_z \tau_z = C = \pm 1$, with the TBG flat-band dispersion mapping onto weak tunneling between the two copies. Thus, in the absence of dispersion and with full sublattice polarization, there is then a U(4) × U(4) symmetry coming from each "ZLL." Therefore, much intuition from the theory of U(4) quantum-Hall ferromagnetism in MLG [26] can be translated to TBG, albeit with the novel twist of time-reversal symmetry: Unlike a single ZLL, unfrustrated Cooper pairs can form from one electron in each copy.

This doubled-ZLL picture also brings us back to the tension between the QH and Hubbard paradigms. In the end, TBG is a novel hybrid of both: Within each copy of the ZLL, the electrons prefer to polarize into a subset of the four components by direct analogy to U(4) QH ferromagnetism. However, the tunneling-induced coupling *between* the two ZLLs couples their order parameters via an antiferromagnetic "t^2/U" superexchange, which picks out a submanifold of states comprised of the K-IVC and the valley-Hall (VH) state. Finally, taking into account the finite sublattice polarization, the K-IVC state that remains a "generalized ferromagnet" is favored relative to the valley-Hall state.

II. HAMILTONIAN AND SYMMETRIES

Our starting point is the Bistritzer-MacDonald (BM) [1,2] model of twisted bilayer graphene, which considers two graphene layers with a relative twist angle θ coupled via a slowly varying moiré potential. The interlayer moiré potential is specified by two parameters, w_0 and w_1, denoting intra- and intersublattice coupling, respectively. The ratio w_0/w_1, which was taken to be 1 in the original BM model, is reduced in realistic samples to about 0.75 due to lattice relaxation effects, which shrink the AA stacking regions relative to the AB regions [27,28]. In the extreme limit where $w_0 = 0$, an extra chiral symmetry is present, which leads to several interesting features including perfectly flat bands at the magic angle [29].

Let us now define an extended BM Hamiltonian, which includes interactions. The interaction is taken to be a double-gate screened Coulomb interaction with $V_q = 2\pi \tanh(|q|d)/\epsilon|q|$, where d is the distance to the gate and ϵ a dielectric constant (similar results are also obtained for the single-gate screened case). Next, we choose a subset of bands of the BM Hamiltonian h_{BM} near charge neutrality labeled by the band index $N_- \leq n \leq N_+$ and assume that all states with $n > N_+$ $(n < N_-)$ are empty (full). The projected Hamiltonian has the form

$$\mathcal{H}_{\text{eff}} = \sum_{k \in \text{BZ}} c_k^\dagger h(k) c_k + \frac{1}{2A} \sum_q V_q : \rho_q \rho_{-q} :, \qquad (1)$$

$$\rho_q = \sum_{k \in \text{BZ}} c_k^\dagger \Lambda_q(k) c_{k+q}, \qquad [\Lambda_q(k)]_{\alpha,\beta} = \langle u_{\alpha,k} | u_{\beta,k+q} \rangle, \qquad (2)$$

where $c(k)$ is a vector of annihilation operators in the combined index $\alpha, \beta, \ldots$ containing spin $s = \uparrow, \downarrow$, valley $\tau = K, K'$, and band $n = N_-, \ldots, N_+$ indices, and $u_\alpha(k)$ are the eigenstates of the BM Hamiltonian. Note that A is the area, and $h(k)$ is the single-particle Hamiltonian, which includes the BM Hamiltonian as well as band renormalization effects due to the exchange interaction with the filled remote bands (see Supplemental Material for details [30]) [10,12,35]. We neglect electron-phonon interactions as well as the short-distance Coulomb scattering $V_{K-K'}$ between the Dirac points, both of which are suppressed by powers of the lattice-to-moiré scale $a/L_M \ll 1$. We refer to these neglected terms as the "intervalley-Hunds" terms.

Since the competing $\nu = 0$ states are distinguished by their broken symmetries, let us review the symmetries of the extended BM Hamiltonian. Letting σ_z, τ_z denote sublattice (A/B) and valley (K/K'), H_{eff} has the following symmetries: (i) $C_2 = \sigma_x \tau_x$ and (ii) $\mathcal{T} = \tau_x \mathcal{K}$, which relate the two valleys, (iii) $C_3 = e^{-(2\pi i/3)\sigma_z \tau_z}$, which acts within each valley, and (iv) $U(2)_K \times U(2)_{K'} \simeq U_C(1) \times U_V(1) \times SU(2)_K \times SU(2)_{K'}$, where $U_C(1)$ and $U_V(1)$ denote charge conservation and valley charge conservation, and $SU(2)_{K,K'}$ represent independent spin rotations in the K and K' valleys. In addition, the BM Hamiltonian has an approximate (v) particle-hole symmetry $\mathcal{P} = i\sigma_x \mu_y \mathcal{K}$ at small angles, where μ_i are the Pauli matrices acting on the layer index [21,36].

The intervalley-Hunds terms, whose magnitude is of the order $J_H \sim 0.2$–0.5 meV, break the independent spin rotations in each valley down to the physical global spin rotation symmetry: $SU(2)_K \times SU(2)_{K'} \to SU(2)$. This effect occurs at order $a/L_M \propto \theta$. Furthermore, umklapp processes that scatter three electrons between the two valleys (either due to phonons or higher-order Coulomb scattering) break $U_V(1)$ down to $\mathbb{Z}_3$ and are suppressed by a further factor of θ^2 [37,38].

III. HARTREE-FOCK MEAN FIELD

In the Hartree-Fock (HF) method, we solve for the set of self-consistent ground-state Slater determinant states characterized by the one-electron density matrices $P_{\alpha,\beta}(k) = \langle c_\alpha^\dagger(k) c_\beta(k) \rangle$. Similar to Refs. [10,11,13], we take both the flat bands and a range of remote bands around charge neutrality into account. However, in contrast to previous studies [10–13], we allow for coherence between the two valleys, which spontaneously breaks the $U_V(1)$ symmetry (see also Ref. [6] for an early suggestion of a different IVC order motivated on phenomenological grounds). Further details of our procedure are provided in the Supplemental Material [30].

The numerical results at CN ($\nu = 0$) are given in Fig. 2 for fixed $\theta = 1.05°$, $\epsilon = 7$ and 12, and $w_0 = 40$ and 80 meV as a function of w_1. Since the magic-angle condition depends on the ratio w_1/θ [2], changing w_1 is approximately equivalent

to changing θ. We exploit this fact to plot the HF energies as a function of an "effective" angle $\tilde{\theta} \equiv 1.05° \times (110/w_1[\text{meV}])$, where $w_1 = 110$ meV is the magic-angle condition for the parameters we have used. From comparison with *ab initio* methods, the magnitudes of the interlayer tunneling terms are estimated to be $w_1 \sim 110$ meV and $w_0 \sim 80$ meV [2,27,28]. Here, we consider a range of values of $w_{0/1}$ that can be far from these estimates as this provides valuable information when comparing numerical results with our analytical findings below.

Depending on the initial condition or which symmetries are explicitly enforced, we find several self-consistent solutions that can be grouped into three categories: (i) a semimetallic (SM) state that preserves C_2, $\mathcal{T}$, and $\text{U}_V(1)$ but *may* break C_3 (this state can be understood as a renormalized version of the BM semimetallic band structure); (ii) a QH insulator with Chern number ± 4 that breaks $\mathcal{T}$ but preserves C_2 and $\text{U}_V(1)$; and (iii) several insulating states with Chern number 0, including the VH state, which breaks C_2 but preserves $\mathcal{T}$ and $\text{U}_V(1)$, the valley-polarized (VP) state [39], which breaks $\mathcal{T}$ and C_2 but preserves $C_2\mathcal{T}$ and $\text{U}_V(1)$, and an IVC state, which breaks $\mathcal{T}$ and $\text{U}_V(1)$ but preserves the combination $\mathcal{T}' = \tau_y\mathcal{K}$, which acts as a spinless Kramers time-reversal symmetry between valleys. Unlike previously studied IVC states in TBG [40] and related moiré materials [41,42], this Kramers IVC (K-IVC) takes place between wave functions that have the *same* Chern number, thus evading the energy penalty associated with vortices in the order parameter [40].

The competition between the VH, VP, QH, and SM states, which were all found in previous mean-field studies [10–12], is very sensitive to the values of (w_0, w_1), which explains why these studies, all of which assumed unbroken $\text{U}_V(1)$ symmetry, did not agree on the nature of the ground state. On the other hand, the $\text{U}_V(1)$-breaking K-IVC state is always the lowest-energy state regardless of the values of w_0, w_1, and ϵ. Another salient feature is that the competition between the K-IVC, QH, and VH is closest when $w_0 \to 0$, but it is lifted in favor of the K-IVC order for larger w_0. The reason for this feature will become clear from our analysis of the approximate symmetries.

The HF numerics shown in Fig. 2 were obtained by keeping six bands per spin and valley, but more generally, we find that mixing between the flat and remote bands only has a quantitative effect over the range of parameters considered. In particular, the K-IVC insulator remains the ground state as more bands are included, and the magnitude of the IVC order parameter remains almost unchanged (Fig. 3), indicating that the symmetry breaking occurs predominantly in the flat bands. The charge gap decreases quantitatively as more bands are included, but it saturates at a value of about 26 meV when 16 bands per spin and valley are taken into account, and a value of $\epsilon = 7$ is used. As a result, our numerical results can be reproduced to a good degree of accuracy within the two-band
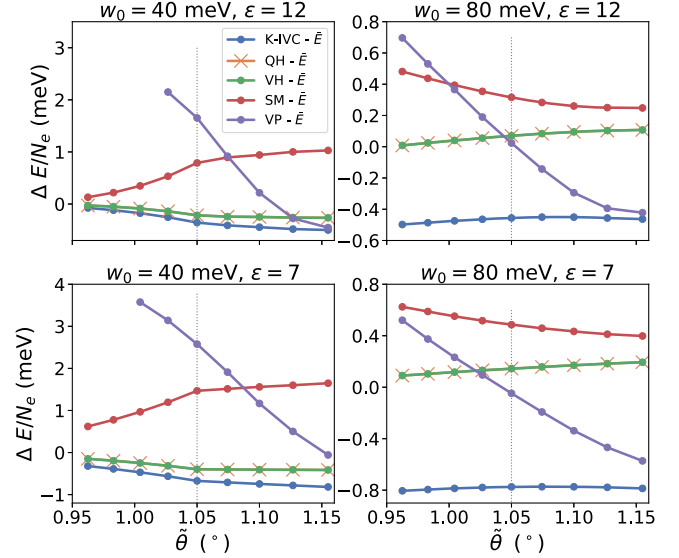

FIG. 2.   Energies per electron at charge neutrality in the K-IVC, QH, VH, SM, and VP states relative to the average energy of the K-IVC, QH, VH, and SM (denoted as $\bar{E}$). Results are obtained at $\theta = 1.05°$ as a function of $100 \le w_1 \le 120$ [meV] (x axis) for $w_0 = 40$ and 80 meV and $\epsilon = 7$ and 12. For convenience, we *define* $\tilde{\theta} = 1.05° \times (110/w_1[\text{meV}])$ in order to convert w_1 to a qualitatively equivalent angle. The dashed vertical line shows the first magic angle. Results were obtained using six moiré bands per spin and valley, and a 24×24 momentum grid. Note that the energies of the VH and QH states are numerically identical.

projection of Ref. [12], where the effect of the remote bands is incorporated only via the exchange renormalization of $h(\boldsymbol{k})$.

A better intuition for the symmetry-breaking phases in Fig. 2 can then be obtained by restricting ourselves to
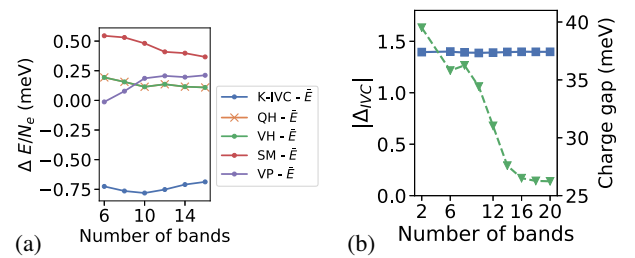

FIG. 3.   (a) Energies per electron in the flat bands of the K-IVC, QH, VH, SM, and VP states relative to the average energy of the K-IVC, QH, VH, and SM (denoted as $\bar{E}$), as a function of the number of bands per spin and valley kept in the Hartree-Fock numerics. (b) IVC order parameter $|\Delta_{\text{IVC}}| = \sum_k \text{tr}(P_{\text{IVC}}(\boldsymbol{k})^2)^{1/2}/N_M$, where $P_{\text{IVC}}(\boldsymbol{k})$ is the $\text{U}_V(1)$-breaking part of $P(\boldsymbol{k})$ and N_M the number of moiré unit cells (left, blue squares). We show the charge gap (right, green triangles) at charge neutrality as a function of the number of bands per spin and valley. The results in both panels (a) and (b) were obtained on a 12×12 momentum grid with $\theta = 1.05°$, $w_0 = 80$ meV, $w_1 = 110$ meV, and $\epsilon = 7$. Note that the energies of the VH and QH states are numerically identical.

the flat bands, where $P(\boldsymbol{k})$ is an 8×8 matrix, which we parametrize as $P(\boldsymbol{k}) = \frac{1}{2}[1 + Q(\boldsymbol{k})]$, with $Q(\boldsymbol{k})^2 = 1$ and $\mathrm{tr} Q(\boldsymbol{k}) = 2\nu$. Furthermore, rather than working in the basis that diagonalizes h_{BM}, it is convenient to work in the sublattice-polarized basis that diagonalizes the sublattice operator $\sigma_{mn}(\boldsymbol{k}) = \langle u_n(\boldsymbol{k})|\sigma_z|u_m(\boldsymbol{k})\rangle$, with $n, m \in \{1, 2\}$ restricted to the two flat bands. This basis is well defined as long as the eigenvalues of the matrix $\sigma(\boldsymbol{k})$ are nonzero, indicating finite sublattice polarization. In the Supplemental Material [30], we check that this is indeed the case. The eight flat bands are then labeled by $s_z = \uparrow/\downarrow$, $\tau_z = K/K'$, $\sigma_z = A/B$. A crucial feature of this basis is that each band carries a quantized Chern number $C = \tau_z \sigma_z$ [29,40,43,44].

With this basis in hand, we can concisely summarize the competing insulators: $Q_{\mathrm{QH}} = \sigma_z \tau_z = C$ (which explains its net Hall conductance); $Q_{\mathrm{VP}} = \tau_z$; $Q_{\mathrm{VH}} = \sigma_z = \tau_z C$ (which explains its valley-Hall conductance); and finally,

$$Q_{\mathrm{K\text{-}IVC}} = \sigma_y[\cos(\theta_{\mathrm{IVC}})\tau_x + \sin(\theta_{\mathrm{IVC}})\tau_y], \qquad (3)$$

which was found to be the ground state at charge neutrality for the entire parameter range that was studied. Under (graphene-scale) lattice translations, the K-IVC order parameter transforms as $\theta_{\mathrm{IVC}} \to \theta_{\mathrm{IVC}} + (2\pi/3)$, while under spinless $\mathcal{T}$, $\theta_{\mathrm{IVC}} \to \theta_{\mathrm{IVC}} + \pi$. In addition to the spin-singlet variant of the K-IVC state discussed here, there are other K-IVC states with different spin structures which are all degenerate on the level of $\mathcal{H}_{\mathrm{eff}}$. These states will be discussed below in the sections containing our analytical results.

IV. APPROXIMATE SYMMETRY AND HIERARCHY OF ENERGY SCALES

A. Enlarged U(4) × U(4) symmetry

Below, we show how a large U(4) × U(4) symmetry appears in the pure interaction model (i.e., with no dispersion) in the chiral limit. We begin by showing that even away from the chiral limit, the flat-band-projected interaction term has an enhanced U(4) symmetry. Next, we show that the chiral model also has a different enhanced U(4) symmetry, even when dispersion is included. Combining these symmetries, we obtain a large U(4) × U(4) symmetry for the chiral model in the absence of dispersion.

Motivated by the numerical result, in the following, we restrict ourselves to the two flat bands (per spin and valley) and rewrite the interacting Hamiltonian (1) as

$$\mathcal{H}_{\mathrm{eff}} = \sum_{\boldsymbol{k}} c_{\boldsymbol{k}}^\dagger \tilde{h}(\boldsymbol{k}) c_{\boldsymbol{k}} + \frac{1}{2A}\sum_{\boldsymbol{q}} V_{\boldsymbol{q}} \delta\rho_{\boldsymbol{q}} \delta\rho_{-\boldsymbol{q}} + \mathrm{const}, \quad (4)$$

$$\delta\rho_{\boldsymbol{q}} = \rho_{\boldsymbol{q}} - \bar{\rho}_{\boldsymbol{q}}, \qquad \bar{\rho}_{\boldsymbol{q}} = \frac{1}{2}\sum_{\boldsymbol{G}, \boldsymbol{k}} \delta_{\boldsymbol{G}, \boldsymbol{q}} \mathrm{tr} \Lambda_{\boldsymbol{G}}(\boldsymbol{k}), \qquad (5)$$

where the interaction term differs from Eq. (1) by an exchange term due to normal ordering as well as the subtraction of the average charge density at neutrality

$\sum_{\boldsymbol{q}} \bar{\rho}_{\boldsymbol{q}}$ (see Supplemental Material [30] for details). The resulting density operator $\delta\rho_{\mathbf{q}}$ is exactly odd under particle-hole symmetry, and hence $\tilde{h}$ and the interaction are *separately* particle-hole symmetric ($\sum_{\boldsymbol{q}} \bar{\rho}_{\boldsymbol{q}}$ is the total charge density of the flat bands).

Let us first consider the limit where sublattice polarization is not saturated, i.e., chiral symmetry is not present, $w_0 \neq 0$. Now, the particle-hole symmetry of the projected Hamiltonian (4) has important consequences. This case follows from the observation that a $\mathcal{PT}$ symmetry (which flips energy but not momentum) is equivalent, within a perfectly flat band (i.e., on *ignoring* the single-particle dispersion), to a single-particle *unitary* symmetry since it leaves the space of eigenstates invariant. In our model, the gauge can be chosen such that the $\mathcal{PT}$ symmetry has the following simple form in the flat-band-projected basis (see Supplemental Material [30])

$$i\mathcal{PT} = \tau_y \sigma_y. \qquad (6)$$

Note that $\mathcal{PT}$ acts locally in space and momentum but exchanges valley and sublattice, relating flat bands with the same Chern number $C = \tau_z \sigma_z$. Thus, if we neglect the dispersion term $\tilde{h}$, we find that the $U(2)_K \times U(2)_{K'}$ of the Hamiltonian is enlarged to a $U(4)_{\mathcal{PT}}$ symmetry whose generators are $\{t^a, t^a \sigma_y \tau_y\}$, where t^a are the eight (sublattice and valley diagonal) generators $t^a = \{s_\mu, \tau_z s_\mu\}$ of $U(2)_K \times U(2)_{K'}$ and $\mu = \in \{0, 1, 2, 3\}$. This unitary symmetry is broken by the dispersion term $\tilde{h}$, which anticommutes with the extra generators $t^a \sigma_y \tau_y$.

Another limit where the symmetry of the Hamiltonian is enhanced is the chiral limit $w_0 = 0$ [29,45], where the BM Hamiltonian has an extra chiral symmetry $\mathcal{S} = \sigma_z$, $\{\mathcal{S}, H_{\mathrm{BM}}\} = 0$, leading to complete sublattice polarization. In this case, we can combine $\mathcal{PT}$ symmetry with $\mathcal{S}$ to obtain a $\mathbb{Z}_2$ unitary symmetry R given by

$$R = \mathcal{PTS} = \tau_y \sigma_x. \qquad (7)$$

Similar to $\mathcal{PT}$, R acts locally in space and momentum but exchanges the valley and sublattice, relating bands with the same Chern number $C = \tau_z \sigma_z$. Its existence enlarges the symmetry of the model to $U(4)_R$, whose generators are $\{t^a, t^a R\}$. It is important to notice that this $U(4)_R$ symmetry is different from the $U(4)_{\mathcal{PT}}$ symmetry discussed earlier. In addition, the $U(4)_R$ symmetry is preserved when including the dispersion $\tilde{h}$ and does not rely on the flat-band projection; i.e., it is a symmetry of the full Hamiltonian in the chiral limit.

Combining the two previous discussions, we find that the interaction in the chiral limit has a large U(4) × U(4) symmetry whose generators are $\{t^a, t^a \tau_y \sigma_x, t^a \tau_y \sigma_y, t^a \sigma_z\}$. An intuitive understanding of this result is obtained by observing that in the chiral limit, the form factor $\Lambda_{\boldsymbol{q}}(\boldsymbol{k})$ has the remarkably simple form
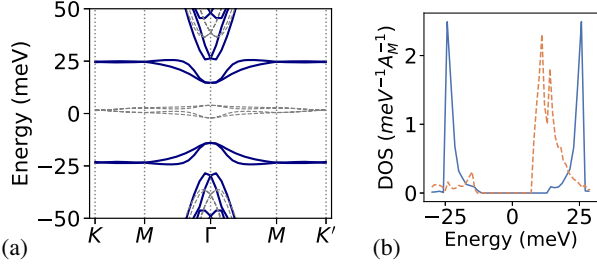
FIG. 4.   (a) HF band spectrum of the K-IVC state that solves the self-consistency equations when six bands per spin and valley are used. The parameters were $\theta = 1.05°$, $w_0 = 78\,\mathrm{meV}$, $w_1 = 105\,\mathrm{meV}$, and $\epsilon = 9.5$. The gray dashed lines correspond to the original BM band spectrum. (b) DOS of the K-IVC state at charge neutrality (solid blue line) and the self-consistent HF solution with empty flat bands, i.e., at filling $\nu = -4$ (dashed orange line). Here, A_M is the area of the moiré unit cell.
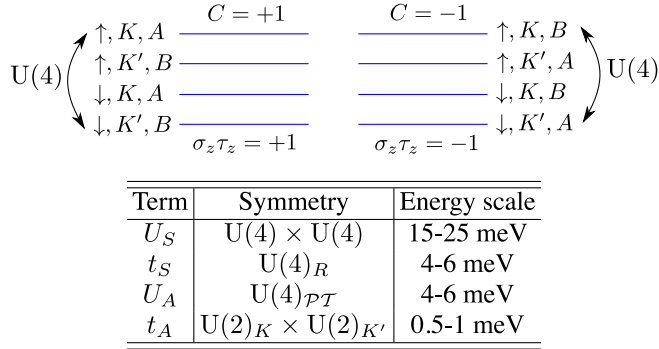

FIG. 5.   Illustration of the U(4) × U(4) symmetry associated with the symmetric part of the interaction $\mathcal{H}_S$. The symmetry corresponds to arbitrary rotations among bands with the same Chern number (top panel). A table illustrating the hierarchy of energy scales and the different symmetries associated with each scale is shown in the bottom panel. Here, U(4)$_\eta$ denote the U(4) subgroup of unitary matrices in U(4) × U(4) commuting with η.

$$\Lambda_q(\boldsymbol{k}) = F_q(\boldsymbol{k}) e^{i\Phi_q(\boldsymbol{k})\sigma_z\tau_z}, \tag{8}$$

where $F_q(\boldsymbol{k})$ and $\Phi_q(\boldsymbol{k})$ are two real scalars whose properties are discussed in more detail in the Supplemental Material [30]. As a result, the interaction is invariant under any unitary rotation that commutes with $\sigma_z\tau_z$, yielding the symmetry U(4) × U(4) corresponding to arbitrary unitary rotations that relate flat bands with the same Chern number, as illustrated in Fig. 5.

B. Hierarchy of energy scales

In the realistic case where $w_0 \neq 0$ and $\tilde{h}$ are not negligible, we can estimate the strength of the U(4) × U(4) symmetry breaking by splitting the form factor $\Lambda_q(\boldsymbol{k})$ into components $\Lambda_q^{S/A}(\boldsymbol{k})$ that commute/anticommute with R. Using the remaining symmetries, one can show (see

Supplemental Material [30]) that $\Lambda_q^S(\boldsymbol{k})$ has the form given in Eq. (8), while $\Lambda_q^A(\boldsymbol{k}) = \sigma_x\tau_z F_q^A(\boldsymbol{k}) e^{i\Phi_q^A(\boldsymbol{k})\sigma_z\tau_z}$. We can now write the density as $\delta\rho_q = \delta\rho_q^S + \delta\rho_q^A$, with $\delta\rho_q^{S/A}$ given by

$$\delta\rho_q^{S/A} = \sum_{\boldsymbol{k}} \left\{ c_{\boldsymbol{k}}^\dagger \Lambda_q^{S/A}(\boldsymbol{k}) c_{\boldsymbol{k}+q} - \frac{1}{2} \sum_{\boldsymbol{G}} \delta_{\boldsymbol{G},\boldsymbol{q}} \mathrm{tr}\Lambda_{\boldsymbol{G}}^{S/A}(\boldsymbol{k}) \right\}. \tag{9}$$

We notice that the R-symmetric component of the density $\delta\rho_q^S$ acts within the same sublattice, whereas the R nonsymmetric part $\delta\rho_q^A$ acts *between* sublattices. This R-breaking component induces a splitting of the interaction into an intrasublattice part $\mathcal{H}_S = (1/2A) \sum_q V_q \delta\rho_q^S \delta\rho_{-q}^S$, which has the full U(4) × U(4) symmetry and an intersublattice part $\mathcal{H}_A = (1/2A) \sum_q V_q [\delta\rho_q^S \delta\rho_{-q}^A + \delta\rho_q^A \delta\rho_{-q}^S + \delta\rho_q^A \delta\rho_{-q}^A]$ with only a U(4) symmetry. Similarly, the form of the dispersion $\tilde{h}$ is restricted by symmetries to

$$\tilde{h}(\boldsymbol{k}) = h_0(\boldsymbol{k})\tau_z + h_x(\boldsymbol{k})\sigma_x + h_y(\boldsymbol{k})\sigma_y\tau_z, \tag{10}$$

with the R-symmetric (nonsymmetric) part given by $h_{x,y}(\boldsymbol{k})$ [$h_0(\boldsymbol{k})$]. Note that, unlike the interaction, the symmetric part acts between sublattices, and the nonsymmetric part acts within each sublattice.

Let us denote the typical energy scales associated with $\mathcal{H}_S$, $\mathcal{H}_A$, $h_{x,y}(\boldsymbol{k})$, and $h_0(\boldsymbol{k})$ by U_S, U_A, t_S, and t_A, respectively (see Supplemental Material for details [30]). One crucial observation is that even though the realistic value of w_0/w_1 is not small, the R-breaking terms U_A and t_A are smaller than their R-symmetric counterparts U_S and t_S by a factor of 3–5, as shown numerically in the Supplemental Material [30] and summarized in Fig. 5. Furthermore, even after accounting for the band renormalization effects, the dispersion t_S is, on average, smaller by a factor of 3–5 compared to the interaction.

The previous discussion points to a hierarchy of energy scales associated with different symmetries. The largest scale is associated with the intrasublattice interaction $\mathcal{H}_S$, which has the enlarged symmetry U(4) × U(4) implemented by unitary rotations that commute with $\sigma_z\tau_z$. This symmetry is broken at lower energy scales by two different terms. First, the intersublattice $h_{x,y}$ breaks it down to a single U(4)$_R$ that commutes with σ_x, corresponding to the symmetry of the chiral model discussed earlier. Second, the intersublattice interaction $\mathcal{H}_A$ breaks it down to a different U(4)$_{\mathcal{PT}}$ subgroup that commutes with $\sigma_x\tau_z$. The presence of both terms thus reduces the symmetry down to U(2)$_K$ × U(2)$_{K'}$, which is the intersection of the two U(4) subgroups. The intrasublattice dispersion h_0 is smaller in magnitude (~0.5–1 meV) and does not break the symmetry any further, so it can be neglected. Finally, the intervalley-Hunds coupling breaks the symmetry down to U$_C$(1) × U$_V$(1) × SU(2) at smaller scales. Close to the

magic angle, all the scales are governed by the interaction and depend crucially on the structure of the wave functions [via $\Lambda_q(\boldsymbol{k})$] rather than the detailed $\boldsymbol{q}$ dependence of V_q.

V. GROUND STATE AT EVEN INTEGER FILLING

A. Energetics and ground state of the spinless model

To understand the competition between different states, it is instructive to start by considering the simpler problem of spinless electrons at half-filling, for which we simply need to replace U(4) → U(2) in the discussion above. Physically, this process is equivalent to assuming a spin-unpolarized solution at CN or a spin-polarized solution at half-filling.

We take the strong-coupling limit by assuming that the intrasublattice interaction scale is much larger than the other scales, i.e., $U_S \gg U_A, t_S$, and subsequently solve for the ground states in this limit. For the realistic parameters, U_S is only a factor of 3–5 larger than U_A and t_S. However, as we will see, the results of the strong-coupling analysis agree remarkably well with the Hartree-Fock numerics, providing an independent justification for the results beyond mean field. We will comment later on the validity of our results for intermediate coupling, $U_S \sim t_S$.

We start by noting that $\mathcal{H}_S$ is a non-negative definite operator for any repulsive interaction $V_q > 0$, which implies that any state satisfying $\delta\rho_q^S|\Psi\rangle = 0$ for $\boldsymbol{q} \neq 0$ is a ground state [9,35,46]. Next, we note that the diagonal form of $\Lambda_q^S(\boldsymbol{k})$ in the sublattice and valley implies that $\delta\rho_q^S$ annihilates any sublattice or valley "ferromagnet" where two of the four sublattice or valley states shown in Fig. 6 are completely filled. For the $\boldsymbol{q}$ that is not a reciprocal lattice vector, this result follows by noting that the action of $\delta\rho_q^S$ changes an electron's momentum by $\boldsymbol{q}$, which is impossible in a completely filled or empty band. For reciprocal lattice vector $\boldsymbol{q}$, the action of the first term in Eq. (9) on a completely filled or empty band is finite but cancels exactly against the second term at CN, as shown in the Supplemental Material [30]. Simple states satisfying this condition are the QH $\sigma_z\tau_z$, VH σ_z, and VP τ_z states. More general states are obtained by acting with any U(2) × U(2) rotation that commutes with $\sigma_z\tau_z$ on these simple states, yielding a manifold of Slater determinant states labeled by a $\boldsymbol{k}$-independent Q satisfying $[Q, \sigma_z\tau_z] = 0$. They fall into two categories: (i) a U(2) × U(2)-invariant QH state with a total Chern number ± 2 obtained by filling two bands with the same Chern number and (ii) a manifold of zero Chern number states generated by the action of U(2) × U(2) on the VP state. This manifold includes the VH state as well as two distinct types of IVC orders that break $U_V(1)$: the Kramers IVC state $\sigma_y\tau_{x,y}$ discussed earlier and a $\mathcal{T}$-symmetric IVC state with $\sigma_x\tau_{x,y}$. Both IVC states hybridize bands with the same Chern number, and as a result, the order parameter can be uniform in $\boldsymbol{k}$ and evade the energy penalty due to vortices discussed in earlier works [40–42].
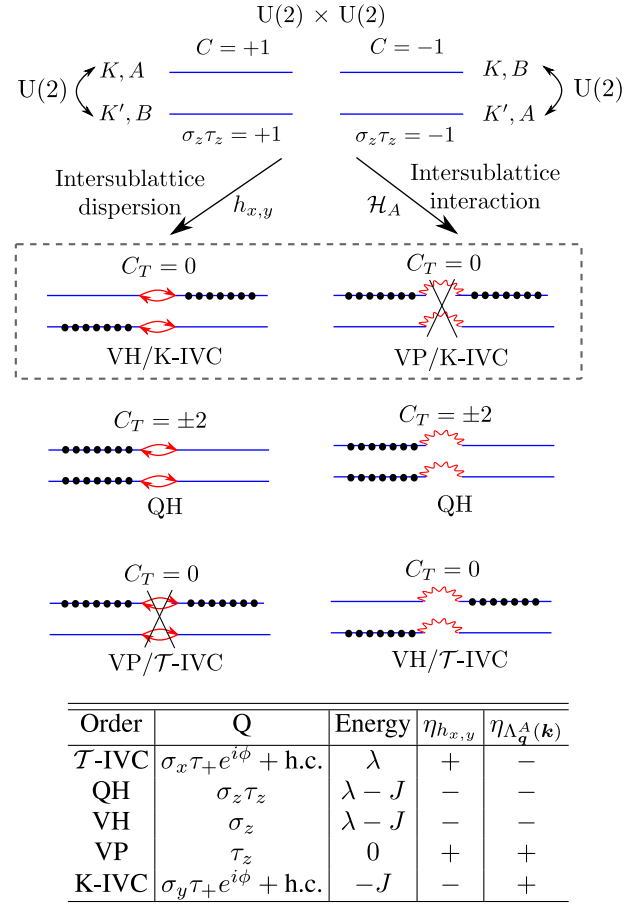

FIG. 6. Schematic illustration of the symmetry reduction and ground-state selection in the spinless model (top panel). Beginning with the U(2) × U(2) symmetric intrasublattice interaction $\mathcal{H}_S$, which allows for free rotations within the two $C = 1$ and two $C = -1$ levels, the symmetry is lowered by the dispersion $h_{x,y}$ (left) and the intersublattice interaction $\mathcal{H}_A$ (right), which splits the degenerate states. The K-IVC insulator is the unique state that is optimal for both perturbations. Table of the low-energy states in the spinless model, showing how their energy is affected by dispersion $h_{x,y} \propto \sigma_x$, $\sigma_y\tau_z$ and finite sublattice polarization $\Lambda_q^A(\boldsymbol{k}) \propto \sigma_x\tau_z, \sigma_y$ (bottom panel). Here, $J \sim t_S^2/U_S$ and $\lambda \sim U_A^2/U_S$ are of the order 1–2 meV, and $\eta_x = +/-$ depending on whether the commutator/anticommutator of Q and x vanishes, i.e., $[Q, x]_{\eta_x} = 0$.

Order	Q	Energy	$\eta_{h_{x,y}}$	$\eta_{\Lambda_q^A(\boldsymbol{k})}$
$\mathcal{T}$-IVC	$\sigma_x\tau_+ e^{i\phi} + $ h.c.	λ	+	−
QH	$\sigma_z\tau_z$	$\lambda - J$	−	−
VH	σ_z	$\lambda - J$	−	−
VP	τ_z	0	+	+
K-IVC	$\sigma_y\tau_+ e^{i\phi} + $ h.c.	$-J$	−	+

Including the dispersion $h_{x,y}(\boldsymbol{k})$ breaks the U(2) × U(2) down to U(2)$_R$. It has the form of an intravalley, intersublattice tunneling with amplitude $h_x(\boldsymbol{k}) + ih_y(\boldsymbol{k})$ connecting pairs of opposite Chern bands, as shown in Fig. 6. Thus, a state in which all pairs of bands connected by $h_{x,y}$ are either both full or both empty is annihilated by $h_{x,y}$ since the tunneling processes are completely blocked. This case is equivalent to $[Q, \sigma_x] = 0$. It can be seen by noting that commutation with both σ_x and $\sigma_z\tau_z$ means that Q is proportional to the identity in the SU(2) pseudospin variable $(\sigma_x, \sigma_y\tau_z, \sigma_z\tau_z)$ whose z component is the Chern

number and whose x, y components correspond to the tunneling $h_{x,y}$; i.e., Q describes a state with zero total pseudospin that is annihilated by the pseudospin flip operators proportional to $h_{x,y}$. For the remaining states, the action of $h_{x,y}$ creates an electron-hole ($e - h$) excitation between these pairs of bands. Since the electron and hole carry opposite Chern numbers, the electron-hole excitations always have a finite energy of the same order as U_S, as shown in the Supplemental Material [30]. This case can be understood by noting that the condensation of such electron-hole pairs is equivalent after a particle-hole transformation to superconducting pairing in a ± 2 Chern band, which is known to be energetically unfavorable [40]. The energy due to the tunneling $h_{x,y}$ can be computed within second-order perturbation theory, leading to an energy reduction of $J \sim t_S^2/U_S \sim 1$–2 meV. This gain, which resembles antiferromagnetic "superexchange," is due to virtual tunneling processes between pairs of bands connected by $h_{x,y}$, which is maximized if only one band is filled in each pair. This requirement is equivalent to the condition $\{Q, \sigma_x\}$, which is satisfied by two types of states: (i) a U(2)-invariant QH state with Chern number ± 2 and (ii) a manifold of states with vanishing Chern number isomorphic to $\mathrm{U}(2)/\mathrm{U}(1) \times \mathrm{U}(1) \simeq S^2$ generated by the VH and K-IVC states, which form a sphere [see Fig. 7(b)].

The intersublattice part of the interaction $\mathcal{H}_A$ breaks $\mathrm{U}(2) \times \mathrm{U}(2)$ to a different $\mathrm{U}(2)_{\mathcal{PT}}$ subgroup. Because the cross terms $\delta\rho_q^S \delta\rho_{-q}^A + \text{H.c.}$ in $\mathcal{H}_A$ are already guaranteed to vanish on the ground-state manifold of $\mathcal{H}_S$, the residual $\delta\rho_q^A \delta\rho_{-q}^A$ is positive definite, and $\mathcal{H}_A$ selects the submanifold of ground states annihilated by $\delta\rho_q^A$. Because of the structure of the intervalley form factor $\Lambda_q^A(k) \propto \sigma_x\tau_z, \sigma_y$, these states satisfy the condition $[Q, \sigma_x\tau_z] = 0$, forming the manifold $\mathrm{U}(2)/\mathrm{U}(1) \times \mathrm{U}(1) \simeq S^2$ generated by the VP and K-IVC. The energy of the other states is increased by an amount of the order $\lambda \sim U_A^2/U_S \sim 1$ meV (see Supplemental Material [30]).

Thus, in the presence of both h_{xy} and $\mathcal{H}_A$, the K-IVC state, which benefits from both perturbations, has the lowest energy followed by the VP and QH/VH (the latter two are degenerate) whose competition is determined by the relative strength of the intersublattice interaction U_A^2/U_S and the energy reduction due to superexchange t_S^2/U_S. This case is consistent with the numerical results in Fig. 2, where the energies of the VP state and the QH/VH state cross as a function of w_1, which controls both $h_{x,y}$ and $\mathcal{H}_A$. At a fixed w_1, decreasing w_0, whose main effect is decreasing $\mathcal{H}_A$, clearly favors the VH/QH states and makes them closer in energy to the K-IVC ground state. The $\mathcal{T}$-IVC state, which was not seen in the numerics, is disfavored by both and has the highest energy.

In the realistic magic-angle parameter regime, the dispersion scale t_S is only a factor of 3–5 smaller than the interaction scale U_S, and some states may become
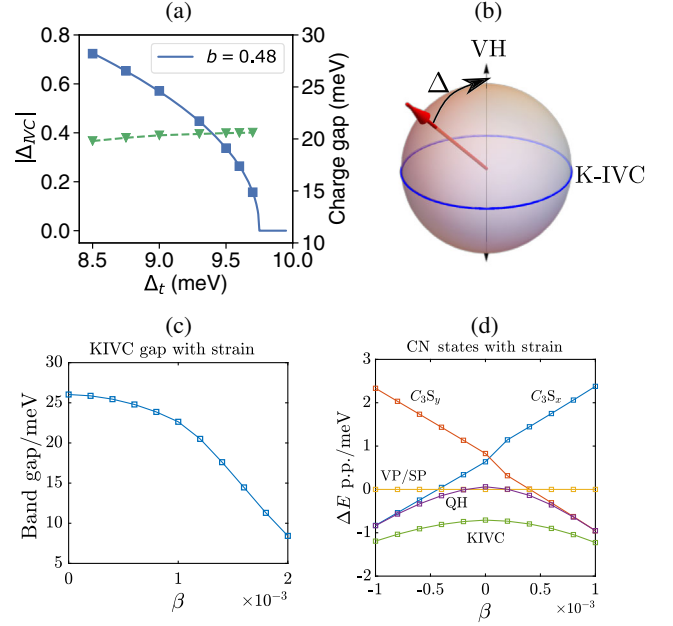

FIG. 7. (a) K-IVC order parameter as a function of the sublattice potential Δ_t on the top layer (blue) fitted to $a(\Delta_{\mathrm{IVC}} - \Delta_{t,*})^b$ with $\Delta_{t,*} = 10.35$ meV, with the gap across the transition shown in green. The curve was computed on a 12×12 momentum grid using the parameters $\theta = 1.05°$, $w_0 = 80$ meV, $w_1 = 98$ meV, and $\epsilon = 12$. (b) Schematic illustration of the manifold of low-energy states for finite Δ. Since the IVC and VH order parameters anticommute, the order parameter is a vector on S^2 that gradually rotates towards the z axis as Δ_t is increased. (c) IVC gap as a function of the C_3-breaking parameter β, with the energies of the different states as a function of β given in panel (d).

energetically competitive by optimizing this part first. Indeed, this result eventually occurs away from the magic angle when the dispersion becomes comparable to the interaction scale. The simplest such states are semimetallic (SM) solutions preserving both $C_2\mathcal{T}$ and $U_V(1)$ [12], which are characterized by

$$Q_{\mathrm{SM}}(k) = \sigma_x e^{i\phi(k)\sigma_z\tau_z} \tag{11}$$

away from the isolated k points at which the gap vanishes where the phase $\phi(k)$ winds by $\pm 2\pi$. Such SM states also break C_3 for realistic values of the parameters w_0 and w_1 [12]. Because of the topology of the bands, the phase $\phi(k)$ winds twice around the Brillouin zone, which means it has at least two vortices (assuming a smooth gauge choice). Another way to see this case is by noting that this order parameter can be obtained by condensing electron-hole pairs discussed earlier, thus gaining energetically from the dispersion but paying an energy penalty of about U_S. In fact, at any finite value of t_S, the insulating order parameters corresponding to QH, VH, or K-IVC order (those benefiting from the antiferromagnetic coupling) develop a small

component of about t_S/U_S parallel to Q_{SM} since the corresponding order parameters anticommute. The SM component grows with increasing t_S, which results in a gradual reduction of the gap until $t_S \sim U_S$, where the insulating phase disappears [12]. This result has important implications for the effect of strain on the insulating state as we discuss later.

B. Charge neutrality: Ground state and spin structure

Upon including spin, we can similarly study the manifold of ground states at CN, starting with the states minimizing the intrasublattice interaction $\mathcal{H}_S$ that satisfy $[Q, \sigma_z \tau_z]$. These states are obtained by completely filling four of the eight bands in Fig. 5. Here, h_{xy} selects states satisfying $\{Q, \sigma_x\} = 0$. These states can be divided into three classes: (i) a spin-unpolarized QH state with Chern number ± 4 obtained by filling all four bands with the same Chern number, (ii) a manifold of states with Chern number ± 2 obtained by filling three bands with the same Chern number and one band with opposite Chern number, and (iii) a manifold of states obtained by filling two bands in each Chern number sector. The states in class (ii) are mixed states corresponding, for instance, to a QH state in one spin species and a VH or IVC state in the other, and they form the manifold $U(4)/U(3) \times U(1)$. States in class (iii) include the spin-unpolarized versions of the spinless phases discussed earlier, including the VH and K-IVC states, which form the manifold $U(4)/U(2) \times U(2)$. In contrast, the interaction $\mathcal{H}_A$ selects states satisfying $[Q, \sigma_x \tau_z] = 0$, which include spin- or valley-polarized states as well as spin-unpolarized K-IVC states. However, the spin- or valley-polarized states do not benefit from the dispersion. Thus, combining the effect of the dispersion and $\mathcal{H}_A$, we are left with K-IVC order as the unique state that is maximally stabilized by both perturbations.

Note that the spin-unpolarized K-IVC state is not invariant under the action of $U(2)_K \times U(2)_{K'}$ rotations. Instead, this action generates a manifold of states that are degenerate with respect to $\mathcal{H}_{eff}$. This manifold can be parameterized by a single 2×2 unitary matrix V in spin space with $Q = \sigma_y(\tau_+ V + \tau_- V^\dagger)$, $\tau_\pm = \frac{1}{2}(\tau_x \pm i\tau_y)$. To understand the structure of these states, we write the manifold as $U(2) \simeq U(1) \times SU(2)$, which can be parametrized as $V = e^{i\phi}e^{i(\theta/2)\boldsymbol{n}\cdot\boldsymbol{s}}$. Thus, a given K-IVC state is specified by choosing a spin quantization axis $\boldsymbol{n}$ on S^2 and specifying two $U(1)$ K-IVC phases $\phi \pm (\theta/2)$ for the up and down spins along $\boldsymbol{n}$. However, note that the spin axis $\boldsymbol{n}$ loses meaning for the spin-singlet state $\theta = 0$. The intervalley-Hunds coupling fixes the value of the relative phase θ between the K-IVC states for up and down spins. An antiferromagnetic coupling, perhaps driven by phonons [47], leads to $\theta = 0$. As expected, this is the spin-singlet K-IVC state, where the orbital currents from opposite spins are added. On the other hand, ferromagnetic Hunds coupling leads to $\theta = \pi$, i.e., a spin triplet K-IVC state.

At this special value, the orbital currents of the oppositely directed spins cancel, leaving behind circulating spin currents (see Fig. 1).

C. Half-filling: Ground state and spin structure

While we have largely focused on charge neutrality $\nu = 0$, let us now briefly discuss half-filling, i.e., $\nu = \pm 2$, leaving a more thorough discussion for the future. At half-filling $\nu = -2$ (the case of $\nu = 2$ can be deduced by performing a particle-hole transformation in the conclusions below), the ground states of $\mathcal{H}_S$ are obtained by filling two out of the eight bands encoded by the condition $[Q, \sigma_z \tau_z] = 0$. In contrast to CN, these states are not completely annihilated by the operator $\delta\rho_{\boldsymbol{G}}^S$ for reciprocal lattice vectors $\boldsymbol{G}$. Instead, the action of $\mathcal{H}_S$ on these states yields a constant energy that does not affect their energy competition. However, such a contribution may affect the competition between the $\nu = \pm 2$ insulating states and metallic or superconducting phases emerging from the $\nu = 0$ state. We leave investigating such competition to future works. Within the manifold of ground states of $\mathcal{H}_S$, states can gain energetically from tunneling if at most one out of each pair of bands coupled through $h_{x,y}$ is filled. The resulting states either have (i) Chern number ± 2 such as valley- and sublattice-polarized or spin-polarized QH states [forming the manifold $U(4)/U(2) \times U(2)$] or (ii) Chern number 0 such as the spin-polarized VH or K-IVC states [forming the manifold $U(4)/U(2) \times U(1) \times U(1)$]. Again, the interaction $\mathcal{H}_A$ instead selects states satisfying $[Q, \sigma_x \tau_z] = 0$, which include spin- and valley-polarized states and spin-polarized K-IVC order. The ground-state manifold in the presence of both band dispersion and $\mathcal{H}_A$ is the K-IVC state. The set of nearly degenerate K-IVC states is obtained by acting with $U_K(2) \times U_{K'}(2)$ on the spin-polarized K-IVC state. The resulting manifold is isomorphic to $U(1) \times S^2 \times S^2$, denoting the K-IVC phase and the direction of the spin in each valley, which can be chosen independently. Intervalley-Hunds coupling locks the spin in the two valleys to be either parallel ($J < 0$ ferromagnetic Hunds coupling) or antiparallel ($J > 0$ antiferromagnetic Hunds coupling). In both cases, spatially varying orbital magnetization currents are present. A full Hartree-Fock numerical analysis of this case is left to future work, but it is worth noting that band renormalization effects at half-filling are expected to be larger than at CN, resulting in smaller gaps.

VI. PHENOMENOLOGY AND RESPONSE

A. Phenomenology of the K-IVC

We now comment on the phenomenological consequences of the K-IVC order.

(i) Circulating currents. Fixing a spin species, the lattice-scale current j_{ij} in the K-IVC ground state

manifests a pattern of circulating currents which triples the unit cell, as shown in Fig. 1. The typical current (or, equivalently, the typical magnetization density) is of the order of microamperes, i.e., $j \sim \mu A$. This finding is consistent with the estimate $j \sim e(v_F/a)(a/L_M)^2 \sim 0.7 \ \mu A$ obtained by assuming that each electron in the flat band is circulating at velocity v_F. In the spin-singlet K-IVC state, the two spin species carry the same current, and the state is thus an orbital-magnetization density wave. However, the spin-triplet K-IVC $Q = \mathbf{n} \cdot \mathbf{s}\tau_{x/y}\sigma_y$ is invariant under the usual *spinful* time-reversal operation $TR = is_y\tau_x K$. Hence, the two spin species carry opposite current, and the magnetization cancels—instead, there are circulating *spin* currents.

Nevertheless, both cases triple the unit cell. In the presence of umklapp scattering, this tripling will manifest as small bond distortions or topographic changes reminiscent of a Kekule pattern, which may be observable in atomically resolved STM spectroscopy.

(ii) Landau fan. Because of the $\mathcal{T}'$ Kramers degeneracy, the conduction (valence) bands of the K-IVC insulator (Fig. 4) have a doubly degenerate band minimum (maxima) at the mini-Γ point. Per spin, they consist of a pair of bands, which we label $Z = \pm 1$, which disperse quadratically. Both bands carry trivial C_3 quantum number, and thus, to leading order within a $k.p$ approach, the Hamiltonian for the conduction band minima is

$$H_\Gamma = \frac{(\mathbf{p} - \mathbf{A})^2}{2m^*} + B\left(m_\Gamma \hat{Z} + g_s\mu_B\hbar\frac{s_z}{2}\right) + \mathcal{O}(p^3),$$
$$(12)$$

where m^* is the effective mass, $\nabla \times \mathbf{A} = B$ is the external magnetic field, m_Γ is the orbital magnetization of the bands at the Γ point (which is odd under $\mathcal{T}'$), and g_s is the g factor for the spin. The low-field Landau-level spectrum is thus $\epsilon_N = B[(\hbar e/m^*) (N + \frac{1}{2}) + m_\Gamma Z + g_s\mu_B\hbar(s_z/2)] + \cdots$, with an analogous result for the valence band. Neglecting g_s and the magnetization m_Γ, the Landau fan would thus have a $\nu = \pm 0, 4, 8, \ldots$ degeneracy arising from spin and $\mathcal{T}'$-Kramers degeneracy. With m_Γ, however, this degeneracy splits, $\nu = \pm 0, 2, 4, \ldots$, with the relative strength of the splitting depending on the ratio of $\hbar(e/m^*)$ to m_Γ. Experiments reporting a charge gap at neutrality find oscillations at $\nu = \pm 0, 2, 4, 8, \ldots$ [5], which seemingly combine the two, perhaps because at higher N or B, the $\mathcal{O}(p^3)$ terms become important. Also, one important caveat is that we find the K-IVC band structure around the Γ point to be sensitive to the twist angle, so the above analysis may not always apply. A full quantitative calculation of the quantum oscillations therefore remains as a useful direction for future work.

(iii) $\mathbb{Z}_2$ topology. Remarkably, when restricting to a spin species, the K-IVC state is a topological insulator protected by Kramers time reversal $\mathcal{T}'$ and U(1) charge conservation. This result is expected since it consists of two IVCs with opposite Chern number $(|KA\rangle + |K'B\rangle$ and $|KB\rangle + |K'A\rangle)$ related by $\mathcal{T}'$. However, note that this case does not automatically imply edge states since the fractional translation τ_z involved in $\mathcal{T}'$ may be broken by a rough edge.

(iv) Phase transitions. Finally, on breaking various symmetries, the K-IVC order can be weakened or destroyed as discussed below.

B. Effect of single-particle perturbations

Because of the presence of an enlarged $U(4) \times U(4)$ symmetry that is only broken by relatively small terms that settle the energy competition among a few low-energy states, we expect the ground state to be sensitive to symmetry-lowering perturbations such as sublattice potential, strain, and magnetic field. The presence of a sublattice potential $\Delta\sigma_z$ is associated with alignment with the hBN substrate, which explicitly favors the VH state ($Q = \sigma_z$) over the K-IVC state. Assuming a fixed spin structure ($Q \propto s_0$ or $\mathbf{n} \cdot \mathbf{s}$), the two order parameters anticommute, forming an O(3) vector living on S^2 as shown in Fig. 7. As Δ is increased, this vector rotates towards the z axis (VH) until it points completely along the z direction, restoring $U_V(1)$ symmetry as shown in Fig. 7. As a result, we do not expect this phase transition to be associated with a gap closing in the fermionic sector, which is verified numerically in Fig. 7.

Next, we consider the effect of strain, which influences the noninteracting band structure in two distinct ways [48]. First, it renormalizes the bandwidth, leading to an increase in the magnitude of the single-particle dispersion t_S. As discussed earlier, this process favors the semimetallic solution and has the effect of gradually reducing the gap in the K-IVC solution by increasing the SM component. The second effect of strain is the explicit breaking of C_3 symmetry. This effect can be taken into account phenomenologically following Refs. [12,49] by rescaling one of the moiré hopping parameters by $1 + \beta$. This rescaling introduces explicit C_3 symmetry breaking in the dispersion $h_{x,y}$, resulting in a linear coupling to the energy of the C_3-breaking SM as shown in Fig. 7(d). The VH and K-IVC states will respond to β by increasing their SM component, leading to a *quadratic* decrease of the VH and K-IVC energies and gaps as a function of β, as seen in Fig. 7. With increasing β, the energies of the three orders approach each other, whereas other states such as VP are not affected. It is worth noting that semimetallic behavior in transport can also emerge purely from disorder, even when the ground state of the clean system is insulating [50].

Finally, let us comment briefly on the effect of magnetic field. The Zeeman coupling depends on the spin structure, and its effect on the gap depends nontrivially on the type of low-lying excitations [47]. On the other hand, the orbital effect of the magnetic field can be understood as follows. For an in-plane field, its main effect is to break C_3 symmetry, shifting the Dirac points away from the moiré K and K' points. In this regard, the effect is similar to the C_3-breaking perturbation discussed above, yielding a quadratic decrease of the gap with an in-plane field, which is consistent with the observation of Ref. [4]. On the other hand, an out-of-plane field is associated with a relatively large Chern-Zeeman effect of about $\sigma_z \tau_z$, which shifts the energies of the opposite Chern bands relative to each other. As a result, it is expected to drive a transition to a QH state with Chern number ± 4 at neutrality and ± 2 at half-filling. We leave a more quantitative discussion for the effect of the magnetic field to future works.

VII. CONCLUSIONS

To summarize, based on both numerical and analytical arguments, we propose that the insulating state observed at charge neutrality in pristine MATBG (magic angle twisted bilayer graphene) [5] is the K-IVC state, i.e., an intervalley-coherent state with an emergent spinless Kramers time-reversal symmetry $\mathcal{T}'$. Interestingly, modulo spin degeneracy, the K-IVC state is a nontrivial topological insulator protected by $\mathcal{T}'$. As a result, it does not admit a real-space strong-coupling "Mott" description as long as the locality of time-reversal and valley U(1) symmetries is preserved. In turn, this result suggests that the momentum-space description employed here, which closely parallels multilayer quantum Hall problems, is more suited to MATBG than real-space descriptions [7,8,17,18], at least when restricted to the space of flat bands at integer fillings. It is worth noting that despite some similarities to a previously proposed intervalley-coherent order [9], our state differs in several crucial aspects, such as the absence of time-reversal symmetry and the presence of nontrivial band topology, which forbids a localized Mott description. Spontaneous-magnetization density wave states have been discussed in other settings, notably in the context of the cuprates as the staggered flux [51] and d-density wave states [52] and loop current states [53] (for a recent discussion of loop current states motivated by TBG, see Ref. [54]), and in untwisted bilayer graphene [55,56]. While reminiscent of the state discussed here, an important difference is that the K-IVC order is very weakly coupled to the underlying lattice. Thus, the spontaneously breaking of the enlarged $\mathrm{U}(1)_{\mathrm{valley}}$ symmetry leads to new consequences, including gapless Goldstone modes and emergent Kramers time-reversal symmetry.

One important issue that is worth highlighting is that we do not expect a finite-temperature phase transition into the K-IVC state, even though it breaks the discrete time-reversal symmetry $\mathcal{T}$. The reason is that the time-reversal symmetry breaking is nontrivially intertwined with the breaking of the continuous-valley charge-conservation symmetry. This case can be seen by noting that the presence of the Kramers time-reversal symmetry $\mathcal{T}' = \tau_y K$ implies that there is no order parameter with nonvanishing expectation value in the K-IVC state that breaks $\mathcal{T}$ without breaking U(1) valley charge conservation.

The analytical arguments in favor of the K-IVC state are based on the presence of an approximate $\mathrm{U}(4) \times \mathrm{U}(4)$ symmetry. One consequence of this approximate symmetry is that small perturbations to the BM band spectrum coming from, e.g., h-BN alignment or strain can destroy the K-IVC state and instead give rise to a valley-Hall or semimetallic state at charge neutrality. It is therefore important to have an estimate of the magnitude of these effects in different devices. Our analysis has a natural generalization to doped systems with two additional electrons or holes per moiré unit cell ($\nu = \pm 2$), so we expect a spin-polarized version of the K-IVC state to occur at those fillings. At odd integer fillings, the situation is different. Applying our construction to odd filling inevitably leads to anomalous Hall insulators, which is at odds with the present experimental data in TBG devices that are unaligned with the h-BN substrate. In fact, our analysis points to the possibility of different types of states at odd filling since, unlike the K-IVC states at even filling, no translationally symmetric Slater determinant state takes advantage of all the terms in the Hamiltonian. In addition, band renormalization effects are expected to play a bigger role, particularly at $\nu = \pm 3$ where mixing with remote bands is more likely [10].

The K-IVC state exhibits a very subtle type of symmetry-breaking order, leading to an interesting phenomenology. Depending on the spin texture of the K-IVC state, which is only determined by the small intervalley-Hunds terms, we have put forward a physical interpretation of the K-IVC state as either an "orbital-magnetization density wave" on the atomic scale or a state with circulating spin currents. These types of order are presumably hard to directly detect experimentally, but they leave their imprint on the electronic structure. Proposals for a smoking-gun experiment to identify the K-IVC state is left to future work.

Finally, let us comment briefly on the implications of our findings for superconductivity. The presence of the Kramers time-reversal symmetry $\mathcal{T}'$ has important implications for the nature of superconducting states that are proximate to the K-IVC order. Recall that in conventional superconductors with spin-orbit coupling, the Anderson theorem [57] protects pairing between Kramers time-reversal partners, even in the presence of nonmagnetic impurities. Similarly, superconductivity is expected to remain robust in the presence of K-IVC order, as long as electrons related by the $\mathcal{T}'$ symmetry are being uniformly paired. The K-IVC mean-field band structure indicates that small electron or hole doping will lead to

concentric Fermi surfaces around the Γ point, which are related to one another by $\mathcal{T}'$ symmetry. Hence, a Fermi surface coexisting with K-IVC order can be destabilized by coupling to phonons and/or order parameter fluctuations giving rise to the superconducting state. We leave a more detailed analysis of the nature of the superconducting states and their connection to the K-IVC order for future work.

ACKNOWLEDGMENTS

---

[1] J. M. B. L. dos Santos, N. M. R. Peres, and A. H. C. Neto, *Continuum Model of the Twisted Graphene Bilayer*, Phys. Rev. B **86**, 155449 (2012).

[2] R. Bistritzer and A. H. MacDonald, *Moiré Bands in Twisted Double-Layer Graphene*, Proc. Natl. Acad. Sci. U.S.A. **108**, 12233 (2011).

[3] Y. Cao, V. Fatemi, A. Demir, S. Fang, S. L. Tomarken, J. Y. Luo, J. D. Sanchez-Yamagishi, K. Watanabe, T. Taniguchi, E. Kaxiras *et al.*, *Correlated Insulator Behaviour at Half-Filling in Magic-Angle Graphene Superlattices*, Nature (London) **556**, 80 (2018).

[4] M. Yankowitz, S. Chen, H. Polshyn, Y. Zhang, K. Watanabe, T. Taniguchi, D. Graf, A. F. Young, and C. R. Dean, *Tuning Superconductivity in Twisted Bilayer Graphene*, Science **363**, 1059 (2019).

[5] X. Lu, P. Stepanov, W. Yang, M. Xie, M. A. Aamir, I. Das, C. Urgell, K. Watanabe, T. Taniguchi, G. Zhang, A. Bachtold, A. H. MacDonald, and D. K. Efetov, *Superconductors, Orbital Magnets, and Correlated States in Magic Angle Bilayer Graphene*, Nature (London) **574**, 653 (2019).

[6] H. C. Po, L. Zou, A. Vishwanath, and T. Senthil, *Origin of Mott Insulating Behavior and Superconductivity in Twisted Bilayer Graphene*, Phys. Rev. X **8**, 031089 (2018).

[7] A. Thomson, S. Chatterjee, S. Sachdev, and M. S. Scheurer, *Triangular Antiferromagnetism on the Honeycomb Lattice of Twisted Bilayer Graphene*, Phys. Rev. B **98**, 075109 (2018).

[8] H. Isobe, N. F. Q. Yuan, and L. Fu, *Unconventional Superconductivity and Density Waves in Twisted Bilayer Graphene*, Phys. Rev. X **8**, 041041 (2018).

[9] J. Kang and O. Vafek, *Strong Coupling Phases of Partially Filled Twisted Bilayer Graphene Narrow Bands*, Phys. Rev. Lett. **122**, 246401 (2019).

[10] M. Xie and A. H. MacDonald, *On the Nature of the Correlated Insulator States in Twisted Bilayer Graphene*, Phys. Rev. Lett. **124**, 097601 (2020).

[11] Y. Choi, J. Kemmer, Y. Peng, A. Thomson, H. Arora, R. Polski, Y. Zhang, H. Ren, J. Alicea, G. Refael, F. von Oppen, K. Watanabe, T. Taniguchi, and S. Nadj-Perge, *Electronic Correlations in Twisted Bilayer Graphene Near the Magic Angle*, Nat. Phys. **15**, 1174 (2019).

[12] S. Liu, E. Khalaf, J. Y. Lee, and A. Vishwanath, *Nematic Topological Semimetal and Insulator in Magic Angle Bilayer Graphene at Charge Neutrality*, arXiv:1905.07409.

[13] Y. Xie, B. Lian, B. Jäck, X. Liu, C.-L. Chiu, K. Watanabe, T. Taniguchi, B. A. Bernevig, and A. Yazdani, *Spectroscopic Signatures of Many-Body Correlations in Magic Angle Twisted Bilayer Graphene*, Nature (London) **572**, 101 (2019).

[14] Y. Cao, V. Fatemi, S. Fang, K. Watanabe, T. Taniguchi, E. Kaxiras, and P. Jarillo-Herrero, *Unconventional Superconductivity in Magic-Angle Graphene Superlattices*, Nature (London) **556**, 43 (2018).

[15] A. L. Sharpe, E. J. Fox, A. W. Barnard, J. Finney, K. Watanabe, T. Taniguchi, M. A. Kastner, and D. Goldhaber-Gordon, *Emergent Ferromagnetism Near Three-Quarters Filling in Twisted Bilayer Graphene*, Science **365**, 605 (2019).

[16] M. Serlin, C. L. Tschirhart, H. Polshyn, Y. Zhang, J. Zhu, K. Watanabe, T. Taniguchi, L. Balents, and A. F. Young, *Intrinsic Quantized Anomalous Hall Effect in a Moiré Heterostructure*, arXiv:1907.00261.

[17] J. Kang and O. Vafek, *Symmetry, Maximally Localized Wannier States, and a Low-Energy Model for Twisted Bilayer Graphene Narrow Bands*, Phys. Rev. X **8**, 031088 (2018).

[18] K. Seo, V. N. Kotov, and B. Uchoa, *Ferromagnetic Mott State in Twisted Graphene Bilayers at the Magic Angle*, Phys. Rev. Lett. **122**, 246402 (2019).

[19] J. Ahn, S. Park, and B.-J. Yang, *Failure of Nielsen-Ninomiya Theorem and Fragile Topology in Two-Dimensional Systems with Space-Time Inversion Symmetry: Application to Twisted Bilayer Graphene at Magic Angle*, Phys. Rev. X **9**, 021013 (2019).

[20] H. C. Po, L. Zou, T. Senthil, and A. Vishwanath, *Faithful Tight-Binding Models and Fragile Topology of Magic-Angle Bilayer Graphene*, Phys. Rev. B **99**, 195455 (2019).

[21] Z. Song, Z. Wang, W. Shi, G. Li, C. Fang, and B. A. Bernevig, *All Magic Angles in Twisted Bilayer Graphene Are Topological*, Phys. Rev. Lett. **123**, 036401 (2019).

[22] S. Carr, S. Fang, H. C. Po, A. Vishwanath, and E. Kaxiras, *Derivation of Wannier Orbitals and Minimal-Basis Tight-Binding Hamiltonians for Twisted Bilayer Graphene: First-Principles Approach*, Phys. Rev. Research **1**, 033072 (2019).

[23] Y. Jiang, . Lai, K. Watanabe, T. Taniguchi, K. Haule, J. Mao, and E. Y. Andrei, *Charge Order and Broken Rotational Symmetry in Magic-Angle Twisted Bilayer Graphene*, Nature (London) **573**, 91 (2019).

[24] A. Kerelsky, L. J. McGilly, D. M. Kennes, L. Xian, M. Yankowitz, S. Chen, K. Watanabe, T. Taniguchi, J. Hone, C. Dean, A. Rubio, and A. N. Pasupathy, *Maximized Electron Interactions at the Magic Angle in Twisted Bilayer Graphene*, Nature (London) **572**, 95 (2019).

[25] Y. Xie, B. Lian, B. Jäck, X. Liu, C.-L. Chiu, K. Watanabe, T. Taniguchi, B. A. Bernevig, and A. Yazdani, *Spectroscopic*

Signatures of Many-Body Correlations in Magic-Angle Twisted Bilayer Graphene, Nature (London) **572,** 101 (2019).

[26] K. Nomura and A. H. MacDonald, *Quantum Hall Ferromagnetism in Graphene*, Phys. Rev. Lett. **96,** 256602 (2006).

[27] N. N. T. Nam and M. Koshino, *Lattice Relaxation and Energy Band Modulation in Twisted Bilayer Graphene*, Phys. Rev. B **96,** 075311 (2017).

[28] S. Carr, S. Fang, Z. Zhu, and E. Kaxiras, *Minimal Model for Low-Energy Electronic States of Twisted Bilayer Graphene*, Phys. Rev. Research **1,** 013001 (2019).

[29] G. Tarnopolsky, A. J. Kruchkov, and A. Vishwanath, *Origin of Magic Angles in Twisted Bilayer Graphene*, Phys. Rev. Lett. **122,** 106405 (2019).

[30] See Supplemental Material at http://link.aps.org/supplemental/10.1103/PhysRevX.10.031034 additional details on the hidden approximate symmetry of magic angle graphene, and on the derivation of the effective field theories used in the main text, which includes Refs. [31–34].

[31] J. Jung and A. H. MacDonald, *Accurate Tight-Binding Models for the π Bands of Bilayer Graphene*, Phys. Rev. B **89,** 035405 (2014).

[32] E. Cancès and C. Le Bris, *Can We Outperform the DIIS Approach for Electronic Structure Calculations?*, Int. J. Quantum Chem. **79,** 82 (2000).

[33] K. N. Kudin, G. E. Scuseria, and E. Cancès, *A Black-Box Self-Consistent Field Convergence Algorithm: One Step Closer*, J. Chem. Phys. **116,** 8255 (2002).

[34] C. Fang, M. J. Gilbert, and B. A. Bernevig, *Bulk Topological Invariants in Noninteracting Point Group Symmetric Insulators*, Phys. Rev. B **86,** 115112 (2012).

[35] C. Repellin, Z. Dong, Y.-H. Zhang, and T. Senthil, *Ferromagnetism in Narrow Bands of Moiré Superlattices*, Phys. Rev. Lett. **124,** 187601 (2020).

[36] K. Hejazi, C. Liu, H. Shapourian, X. Chen, and L. Balents, *Multiple Topological Transitions in Twisted Bilayer Graphene Near the First Magic Angle*, Phys. Rev. B **99,** 035111 (2019).

[37] I. L. Aleiner, D. E. Kharzeev, and A. M. Tsvelik, *Spontaneous Symmetry Breaking in Graphene Subjected to an In-Plane Magnetic Field*, Phys. Rev. B **76,** 195415 (2007).

[38] X.-C. Wu, Y. Xu, C.-M. Jian, and C. Xu, *Interacting Valley Chern Insulator and Its Topological Imprint on Moiré Superconductors*, Phys. Rev. B **100,** 155138 (2019).

[39] Depending on the parameters, the VP state can also be metallic as a result of the interaction between the remote bands and the active bands.

[40] N. Bultinck, S. Chatterjee, and M. P. Zaletel, *Anomalous Hall Ferromagnetism in Twisted Bilayer Graphene*, Phys. Rev. Lett. **124,** 166601 (2020).

[41] Y.-H. Zhang, D. Mao, Y. Cao, P. Jarillo-Herrero, and T. Senthil, *Nearly Flat Chern Bands in Moiré Superlattices*, Phys. Rev. B **99,** 075127 (2019).

[42] J. Y. Lee, E. Khalaf, S. Liu, X. Liu, Z. Hao, P. Kim, and A. Vishwanath, *Theory of Correlated Insulating Behaviour and Spin-Triplet Superconductivity in Twisted Double Bilayer Graphene*, Nat. Commun. **10,** 5333 (2019).

[43] L. Zou, H. C. Po, A. Vishwanath, and T. Senthil, *Band Structure of Twisted Bilayer Graphene: Emergent Symmetries, Commensurate Approximants, and Wannier Obstructions*, Phys. Rev. B **98,** 085435 (2018).

[44] J. Liu, J. Liu, and X. Dai, *Pseudo Landau Level Representation of Twisted Bilayer Graphene: Band Topology and Implications on the Correlated Insulating Phase*, Phys. Rev. B **99,** 155415 (2019).

[45] P. San-Jose, J. González, and F. Guinea, *Non-Abelian Gauge Potentials in Graphene Bilayers*, Phys. Rev. Lett. **108,** 216802 (2012).

[46] Y. Alavirad and J. D. Sau, *Ferromagnetism and Its Stability from the One-Magnon Spectrum in Twisted Bilayer Graphene*, arXiv:1907.13633.

[47] S. Chatterjee, N. Bultinck, and M. P. Zaletel, *Symmetry Breaking and Skyrmionic Transport in Twisted Bilayer Graphene*, Phys. Rev. B **101,** 165141 (2020).

[48] Z. Bi, N. F. Q. Yuan, and L. Fu, *Designing Flat Band by Strain*, Phys. Rev. B **100,** 035448 (2019).

[49] Y.-H. Zhang, H. C. Po, and T. Senthil, *Landau Level Degeneracy in Twisted Bilayer Graphene: Role of Symmetry Breaking*, Phys. Rev. B **100,** 125104 (2019).

[50] A. Thomson and J. Alicea, *Recovery of Massless Dirac Fermions at Charge Neutrality in Strongly Interacting Twisted Bilayer Graphene with Disorder*, arXiv:1910.11348.

[51] P. A. Lee, N. Nagaosa, and X.-G. Wen, *Doping a Mott Insulator: Physics of High-Temperature Superconductivity*, Rev. Mod. Phys. **78,** 17 (2006).

[52] S. Chakravarty, R. B. Laughlin, D. K. Morr, and C. Nayak, *Hidden Order in the Cuprates*, Phys. Rev. B **63,** 094503 (2001).

[53] C. M. Varma, *Non-Fermi-Liquid States and Pairing Instability of a General Model of Copper Oxide Metals*, Phys. Rev. B **55,** 14554 (1997).

[54] Yu.-P. Lin and R. M. Nandkishore, *Chiral Twist on the High-T_c Phase Diagram in Moiré Heterostructures*, Phys. Rev. B **100,** 085136 (2019).

[55] L. Zhu, V. Aji, and C. M. Varma, *Ordered Loop Current States in Bilayer Graphene*, Phys. Rev. B **87,** 035427 (2013).

[56] J. W. F. Venderbos, *Symmetry Analysis of Translational Symmetry Broken Density Waves: Application to Hexagonal Lattices in Two Dimensions*, Phys. Rev. B **93,** 115107 (2016).

[57] P. W. Anderson, *Theory of Dirty Superconductors*, J. Phys. Chem. Solids **11,** 26 (1959).